Parameter-free treatment of a layered correlated van der Waals magnet: $CrPS_4$

A. R. Alcantara,[1,2,*] C. Lane,[2] J. T. Haraldsen,[1] and R. M. Tutchton[2]
[1]*Department of Physics, University of North Florida, Jacksonville, Florida 32224, USA*
[2]*Theoretical Division, Los Alamos National Laboratory, Los Alamos, New Mexico 87545, USA*

(Received 24 January 2023; revised 5 September 2023; accepted 3 October 2023; published 20 October 2023)

The electronic and magnetic structure of $CrPS_4$, a two-dimensional (2D) magnetic semiconductor is examined by employing the SCAN meta-GGA density functional. We find the resulting magnetic moment and band gap are in excellent agreement with experiment. From the bulk magnetic configurations, we confirm the experimentally observed A-type antiferromagnetic (A-AFM) ordered ground state with a magnetic moment of 2.78 μ_B per chromium atom and band gap of 1.34 eV. To gain insight into the evolution of the ground state with layers, the total energy of each magnetic configuration is calculated for a variety of thicknesses. Monolayer $CrPS_4$ is predicted to be a ferromagnetic insulator with a band gap of 1.37 eV, and A-AFM for bilayer and trilayer, with band gaps of 1.35 and 1.30 eV, respectively. The electronic structure is reported for the single-, two-, and three-layer and bulk $CrPS_4$. Finally, we explore the optical properties of the 2D structure and report the dielectric tensor components and Kerr parameters for the monolayer.

DOI: 10.1103/PhysRevB.108.155133

I. INTRODUCTION

Recently, several reports of two-dimensional (2D) magnetic materials have appeared in the literature displaying a rich variety of magnetic structures [1], along with a myriad of competing topological and superconducting phases [2,3]. The layer-dependent ferromagnetism exhibited by these compounds, such as CrI_3, offers a pathway for the development of spintronic devices because of their wide tunabilities using doping, electric field, light, and pressure [4]. However, the current workhorse CrI_3 and similar materials are fundamentally limited due to their extreme sensitivity to air [5], requiring special glovebox environments and capping layers to preserve the material properties. Therefore, it is crucial to identify air-stable 2D ferromagnetic (FM) materials to advance the next-generation spintronic, optoelectronic, and future quantum information technologies in general [1].

$CrPS_4$ has recently been singled out due to its intrinsic ferromagnetic ordering in the monolayer [6] and robust air stability [7] like $CrTe_2$ [8–10]. These key properties have prompted a number of experimental [11–21] and theoretical [22–26] studies. Specifically, $CrPS_4$ was found to exhibit canted ferromagnetic order within each van der Waals (vdW) layer. When stacked, no net magnetic moment is admitted for an even number of layers characteristic of an A-type antiferromagnetic (A-AFM) ground state [27]. The large magnetic polarization on each Cr site (2.81 μ_B/Cr) produces a 1.40 eV gap in the electronic states, suggesting $CrPS_4$ is well suited for switching [11] and neuromorphic computing [28] applications.

The limited theoretical works analyzing $CrPS_4$ have found mixed success. Density functional theory (DFT) calculations at the generalized gradient approximation (GGA) level can find the correct A-AFM magnetic ground state; however, the Cr magnetic moments are underestimated (2.58 μ_B/Cr), along with the band gap (0.79 eV) by almost a factor of two [22,27], as expected for Kohn-Sham (KS) theory. To remedy this, a Hubbard U parameter has been applied to the Cr-3d states to yield the correct magnetic moment [23]. Unfortunately, this correction predicts an X-type AFM ground state in contrast with neutron scattering measurements [27] and an exaggerated band gap of 1.66 eV. Due to the sensitivity of this system, there is currently no theoretical treatment that captures the delicate balance between the charge and magnetic degrees of freedom. Thus, making predictions of magnetoelastic coupling, magnetoresistive switching, and magnetic excitations is quite challenging.

In this paper, we present an accurate parameter-free description of the layer-dependent magnetic and electronic properties of $CrPS_4$. Utilizing the recently constructed strongly constrained and appropriately normed (SCAN) meta-GGA density functional, the calculated magnetic moments (magnitude and direction) and electronic band gap are in excellent accord with reported experimental values. Our predicted magnetic ground state is in agreement with neutron diffraction studies, thereby overcoming the failure of the DFT+U framework. Upon exfoliating the bulk crystal, we find the interlayer coupling to be extremely weak, between 36 and 49 meV, with the corresponding electronic bands exhibiting essentially no change in band dispersion with thickness. Finally, the dielectric tensor and Kerr parameters are obtained for the monolayer to stimulate further experimental works.

Computational details

Calculations were carried out by using the pseudopotential projector augmented-wave method [29] implemented in

*n01379386@unf.edu

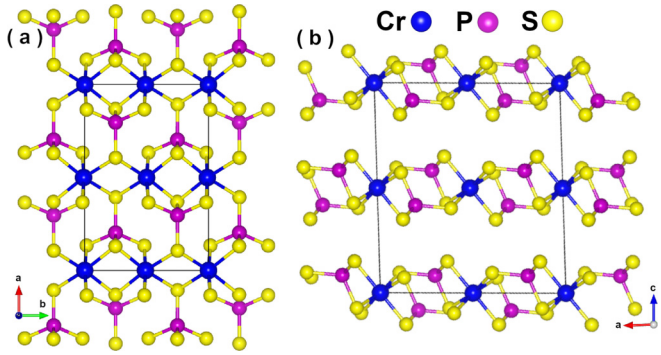

FIG. 1. Supercell of bulk $CrPS_4$ along (a) the c axis and (b) the b axis.

VASP [30,31] with an energy cutoff of 260 eV for the plane-wave basis set. Exchange-correlation effects were treated by using the SCAN meta-GGA scheme [32]. A $6 \times 7 \times 1$ Γ-centered k-point mesh was used to sample the single-, two-, and three-layer structures, whereas a $6 \times 7 \times 5$ mesh was used to sample the bulk material. After a systematic study of k-mesh densities, the $6 \times 7 \times 5$ mesh was found to converge the total energy to within 0.31 meV/Cr. The dielectric tensor components were calculated using 1296 virtual states. Spin-orbit coupling effects were included self-consistently. The $CrPS_4$ unit cell was built using experimentally obtained atomic positions and lattice parameters for the bulk, trilayer, bilayer, and monolayer monoclinic symmetry with a space group $C2/m$ [33]. The magnetism is driven by the Cr^{3+} valence, with three $3d$ electrons spread in the t_{2g} suborbital occupations, yielding a spin moment of $S = \frac{3}{2}$. A vacuum spacing of 19 Å was used to ensure no interactions occur between the periodic images. A total energy tolerance of 10^{-6} eV was used to determine the self-consistent charge density.

II. CRYSTAL STRUCTURE

Figure 1 shows the crystal structure of bulk $CrPS_4$ along the (a) c and (b) b axes. The chromium atoms (blue) sit on an orthorhombic lattice and are octahedrally coordinated by sulfur atoms (yellow) that are slightly distorted off center. Due to the orthorhombic Bravais lattice, the Cr atoms form linear chains of strong intersite coupling along the b axis, with weaker interchain interactions along the a axis. The phosphorus atoms (purple) sit at the center of a sulfur tetrahedral cage, where its position alternates between above and below the Cr layer following the distorted sulfur octahedra. This puckering of the phosphorus sites constrains the primitive unit cell to accommodate four Cr atoms, rather than simply one. Moreover, the phosphorus atoms form a bridge between Cr chains, thereby facilitating the weak interchain interactions. Along the c axis, the atomically thin layers are found to stack in an AA manner with a clear 3.75 Å vdW gap separating neighboring layers. This suggests the electronic states should be predominantly 2D in nature with very weak k_z dispersion.

III. MAGNETIC CONFIGURATIONS AND GROUND STATE

Figures 2(a) and 2(b) show the various collinear commensurate magnetic orders studied in bulk $CrPS_4$, along with the corresponding relative total energies of each magnetic configuration with values from previous PBE [22] and PBE+U ($U = 3$ eV) [23] studies overlayed. Since the bulk primitive cell of $CrPS_4$ has eight Cr atoms spanning two layers, nine distinct commensurate magnetic orders may be accommodated. To enumerate the phases, we initially assume FM coupling between all Cr sites to produce a FM phase with all magnetic moments pointing slightly canted off the c axis. If interchain (intrachain) interactions are switched to AFM, we perturb away from the FM phase yielding a stripelike X-type (Y-, Y′-type) AFM order that varies along the a axis (b axis). Additionally, swapping the FM interlayer coupling for AFM triggers an A-type AFM state where the direction of the magnetic moments alternate with $CrPS_4$ layers. Finally, by combining inter- and intrachain, and interlayer couplings the E-, F-, C-, X′-, and G-type AFM states are found.

Figure 2(b) plots the energy of each magnetic configuration relative to the ground state using PBE [22] (green squares), PBE+U ($U = 3$ eV) [23] (blue circles), and SCAN (red ×) functionals. PBE correctly captures the correct ground-state magnetic order and predicts the FM phase only 2 meV higher

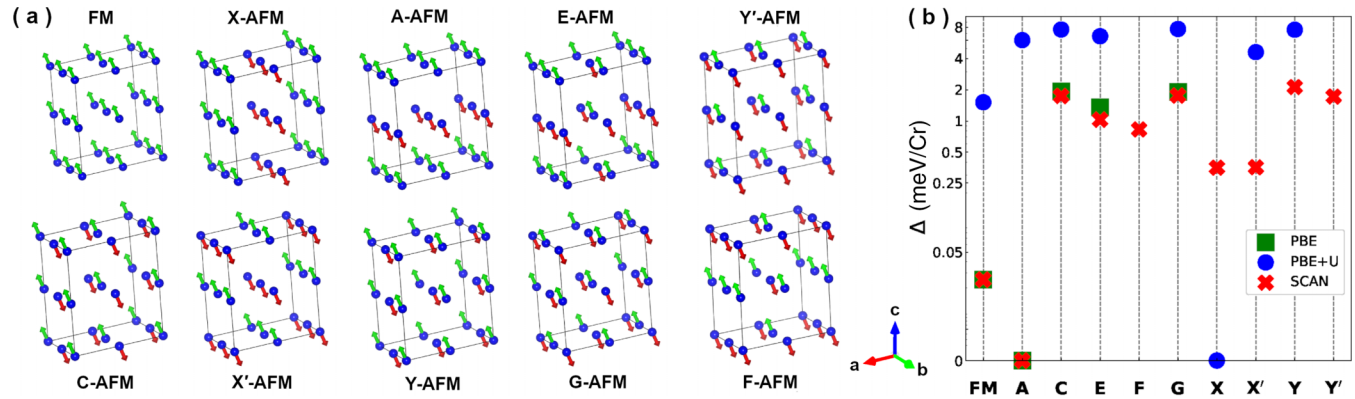

FIG. 2. (a) Ferromagnetic and the nine antiferromagnetic configurations considered for the ground-state ordering of $CrPS_4$. The green and red arrows represent the positive and negative magnetic moments of Cr in the unit cell, respectively. (b) Ground-state energies relative to most stable magnetic configuration by calculated by the PBE (green) [22], PBE+U (blue) [23], and SCAN (red) functionals.

TABLE I. Comparison between experimental and various DFT treatments of the magnetic [6] and electronic [27] properties of bulk $CrPS_4$. The SCAN results (this paper) show improvement over previous PBE [22] and PBE+U ($U = 3$ eV) [23] studies in capturing the experimental values.

Bulk $CrPS_4$	SCAN	Experiment	PBE	PBE+U
Ground state	A-AFM	A-AFM	A-AFM	X-AFM
Band gap (eV)	1.34	1.40	0.79	1.66
Moment (μ_B/Cr)	3.00	2.81	2.58	3.00

in energy. Moreover, the magnetic moment direction and magnitude, though slightly underestimated [Table I], are also in good accord with powder and single-crystal magnetic neutron diffraction results [6]. The remaining magnetic arrangements considered (C-, E-, and G-AFM) are separated from the A-AFM phase by ∼2 eV/Cr, making them irrelevant to the low-energy degrees of freedom. The close energetic proximity of FM and A-AFM states suggests a delicate balance between AFM and FM coupling between the $CrPS_4$ layers. Despite the success of PBE in describing the magnetic state, it severely underestimates the electronic band gap (Table I), as is expected since the KS eigenvalues do not provide the value of the gap. To improve upon the PBE description of the ground state, Joe *et al.* [23] included a Hubbard U of 3 eV on the Cr-d states. By applying a U, charge localization is enhanced on the Cr atomic sites, thereby increasing the magnetic moment and band gap (Table I). Interestingly, the added Hubbard parameter disrupts the ratio of inter- and intralayer exchange couplings, thus predicting a X-AFM ground state with all other phases at least 1.5 eV/Cr higher in energy.

We find the SCAN density functional to remedy the pitfalls of both previous approaches without the introduction of any empirical parameters. Specifically, SCAN recovers the experimental A-AFM ground-state ordering and predicts magnetic moments of 3.00 μ_B tilted off of the c axis by 71.6°, in excellent accord to the experimental powder and single-crystal magnetic neutron diffraction values [6]. Regarding magnetic moments, the values obtained by neutron scattering involve uncertainties since the chromium form factor is not *a priori* known. Note that, when estimating the chromium magnetic moment, we have increased the Wigner-Seitz radius of the integration sphere beyond the default value from 1.323 Å (covalent radius) to 1.74 Å ($\frac{3}{4}$ of the Cr-S bond length) to fully capture the magnetic density centered on the chromium atomic site and the part originating from hybridization between the chromium and sulfur atoms, see Appendix A for more details).

The A-AFM state stabilizes with a band gap of ∼1.34 eV that opens around the Fermi energy of the nonmagnetic system. This gap is in good agreement with optical data [27]. The physical interpretation of the band gap obtained in the ground-state DFT calculations has been the subject of much debate in the literature over the years. We note that, in assessing the physical content of the band gap, one must distinguish between the nature of the effective exchange-correlation potential obtained in the KS [34] and generalized KS (gKS) [35] formalisms underlying the construction of various functionals. Within the KS scheme, one uses the electron density as a variational parameter, thereby yielding KS potentials that are inherently multiplicative and orbital independent. In sharp contrast, the Slater determinate is varied in the gKS formalism; this results in gKS potentials that are orbital dependent and are thus nonmultiplicative. Local spin-density approximation (LSDA)/GGA band structures involve multiplicative effective potentials, while the current and common SCAN implementations involve nonmultiplicative potentials due to the inclusion of the kinetic energy density as an ingredient and thus differ in their basic underlying designs. In this connection, Perdew *et al.* [36] have shown that, for a given density functional, the gKS band gap is equal to the fundamental band gap in the solid, which is defined as the ground-state energy difference between systems with different numbers of electrons. There is thus a firm basis for comparing computed band gaps within the gKS-based SCAN formalism with the experimentally observed band gaps (excluding excitonic effects). The preceding considerations indicate that, as a meta-GGA functional improves the description of the ground state, it will necessarily also lead to improvement in the band gap. To this end, the gKS-based SCAN formalism has demonstrated success in capturing not only the magnetic ground state but the band gap in a wide array of materials including La_2CuO_4 [37–39], $YBa_2Cu_3O_6$ [40], Sr_2IrO_4 [41], and $NiPS_3$ [42]. The SCAN ground state has been shown to yield the key optical transitions in La_2CuO_4 [43] and $NiPS_3$ [44]. Therefore, the comprehensive agreement between magnetic and electronic properties in $CrPS_4$ stems from the reduction in self-interaction error in SCAN as compared with PBE and is not accidental.

TABLE II. Energy differences (ΔE) relative to the predicted ground states of eight magnetic configurations for the bulk, bilayer, and trilayer, and two magnetic configurations for the monolayer.

Magnetic order	Bulk ΔE (meV/Cr) (meV/Cr)	Trilayer ΔE (meV/Cr)	Bilayer ΔE (meV/Cr)	Monolayer ΔE (meV/Cr)
FM	0.031	0.075	0.088	0
A-AFM	0	0	0	—
C-AFM	2.172	2.218	2.235	2.706
E-AFM	1.288	1.312	1.286	—
G-AFM	2.203	2.207	2.266	—
X-AFM	0.442	2.687	2.703	—
X′-AFM	0.445	2.687	2.735	—
Y-AFM	2.672	0.467	0.493	—

Table II presents the relative total energy of each magnetic configuration with respect to the A-AFM state for various sample thicknesses. The A-AFM phase is found to be the ground state for all layered films studied, with robust FM order stabilizing in the monolayer. By comparing the energy of each magnetic state, the FM phase is the closest competing magnetic state, with only ≈2–7 meV/Cr energy separation irrespective of thickness. Curiously, the energy difference between A-AFM and FM arrangements follow a nonmonotonic evolution with the number of $CrPS_4$ layers. Similarly, the remaining magnetic orders farther away from the ground state

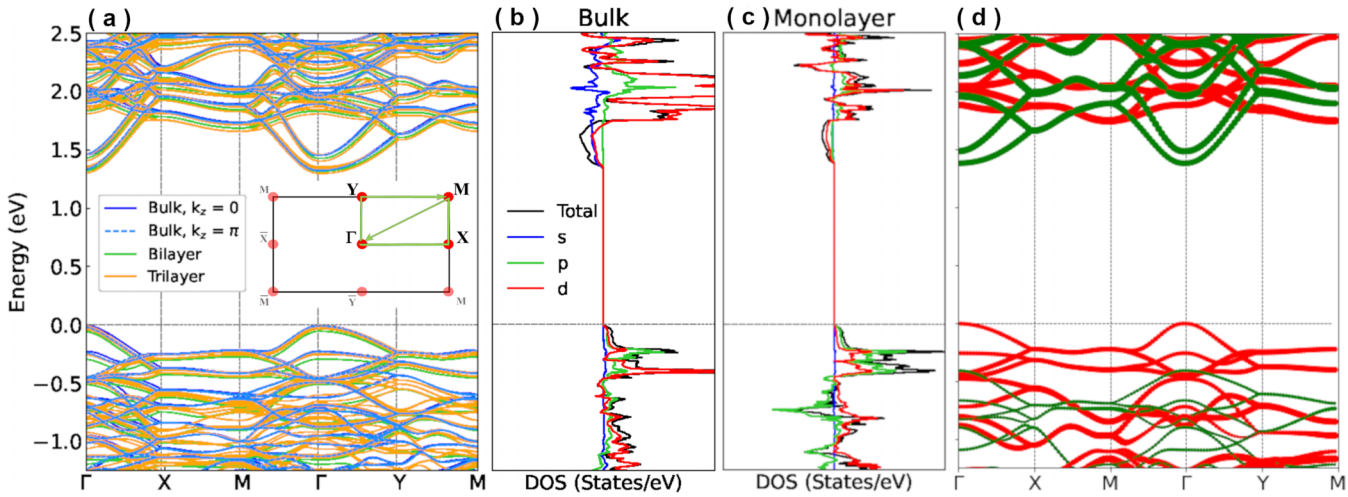

FIG. 3. (a) The electronic band structure and Brillioun zone route explored (inner panel) for the bulk, bilayer, and trilayer. (b) The total and atomically resolved density of states is related next to the band structure for the bulk. (c) Monolayer atomically resolved density of states, with the corresponding (d) monolayer band structure with up (red) and down (green) bands.

display a sensitive dependence on the number of layers. The X- and Y-AFM phases interchange energetic ordering from the bilayer to the bulk systems. This suggests the screening environment may play a key role in tuning the relative strength between the inter- and intrachain interactions. Additionally, by comparing C-, G-, X-, and X′-AFM configurations, the interlayer exchange coupling is found to be on the order of a few meV/Cr.

IV. ELECTRONIC PROPERTIES

Figure 3 shows the (a) electronic band structure and (b) atomically resolved density of states of $CrPS_4$ in the A-AFM phase for the bulk, bilayer, and trilayer, with separately the (c) monolayer atomically resolved density of states and (d) corresponding band structure. For the multilayer structures, the A-AFM magnetic order stabilizes a direct 1.34 eV band gap at Γ in the Brillouin zone of bulk $CrPS_4$. Interestingly, the band dispersions appear to be insensitive to k_z dispersion. Specifically, the bands for $k_z = 0$ (solid blue lines) and $k_z = \pi$ (dashed blue lines) are essentially identical, where small deviations are only exhibited along the M-Γ-Y path in momentum space. The band dispersion along Γ-Z is flat, suggesting the interlayer coupling is weak and each atomically thin layer is relatively electronically isolated, see Appendix B. As $CrPS_4$ is thinned, the band structures for the trilayer (orange solid lines) and bilayer (green solid lines) appear to be stationary and display nearly identical eigenvalues throughout the Brillioun zone, except for a slight rigid shift (∼70 meV) due to the nonmonotonic evolution of the gap. In contrast, the monolayer [Fig. 3(d)] displays an indirect band gap of 1.745 eV characterized by momentum shift of (π, π). The corresponding atomically resolved density of states [Figs. 3(b) and 3(c)] reveals the valence bands to be predominantly composed of sulfur character 99%, whereas the conduction band is dominated by Cr states 27%. This stacking of states follows the Zaanen-Sawatzky-Allen classification of a charge-transfer insulator [45]. Therefore, in contrast with the Mott-Hubbard scenario, when a hole is doped into $CrPS_4$, the carrier would sit on the sulfur atomic sites rather than in the Cr sites. The percentage of metal cation (ligend anion) weight in the conduction (valence) band is relatively constant across the bulk and single- and few-layer systems.

V. OPTICAL PROPERTIES

To accelerate the design of the next-generation microelectronic devices, it is necessary to cross-validate both theoretical calculations and experimental measurements. To this end, we first must judge the quality of our theoretically obtained description of $CrPS_4$. To address this issue, we calculate the dielectric tensor—a key ingredient in the interaction between light and matter—and compare the results with experimental observations.

Figure 4 presents the nonzero matrix elements of the dielectric tensor (real and imaginary components) as a function of energy for a single layer of $CrPS_4$. Two main blocks of transitions are seen spanning ≈2–6 eV and ≈9–11 eV in the imaginary part of the xx and yy tensor components. In contrast, $\varepsilon^{(2)}_{zz}$ displays a very weak leading edge of transitions due to the 2D nature of the material and only retains the broad peak centered at 10 eV. Additionally, the sharp leading edge at ≈2 eV in $\varepsilon^{(2)}$ generates a strong polarization peak in $\varepsilon^{(1)}$ through the Kramer-Kronig relation. On average, the indicated peak structure is in good accord with optical spectroscopy reports [12].

Compared with Fig. 3, the sharp transition edge at ≈2 eV is produced by promoting an electron from the valence- to conduction-band edges along X-M (Y-M). The higher energetic transitions originate from bands 5.0 eV below the Fermi level connecting the flat conduction bands along X-M and Y-M. Furthermore, our theoretically predicted electronic band gap is in very good agreement with the leading edge of the optical conductivity [27]. To allow for future experimental comparison, the refractive index and optical absorption spectrum are provided in Appendix C.

As a consequence of the canted ferromagnetism, the off-diagonal xz component of the dielectric tensor exhibits a

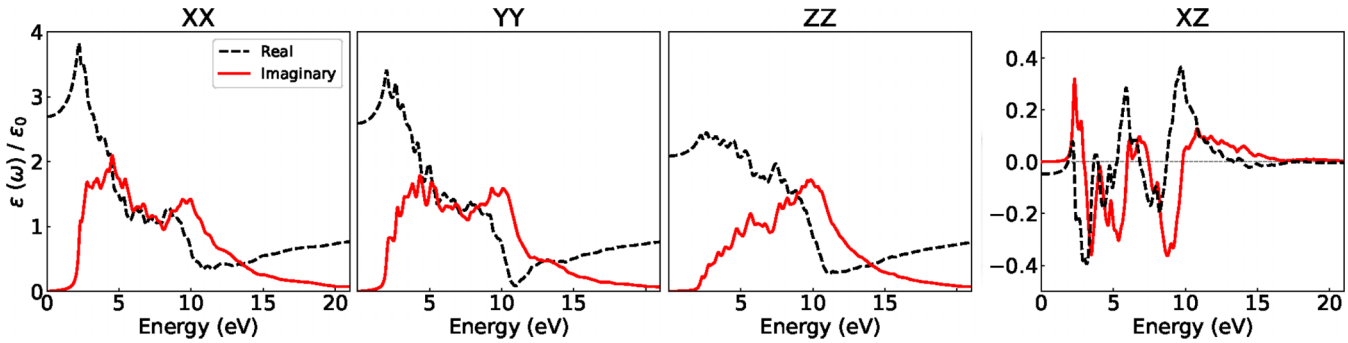

FIG. 4. Dielectric tensor components of $CrPS_4$ ferromagnetic (FM) monolayer showing the real (dashed black line) and imaginary (red) components. The *xy* and *yz* components have little to no contribution to the system.

nonnegligible response. Such a response may induce an appreciable Kerr angle in the polarization of the light reflected from a magnetic $CrPS_4$ layer. This makes the optical Kerr effect particularly useful in giving direct insight into the local, microscopic magnetism [46] and time-reversal symmetry breaking condensed-matter systems in general [47].

To estimate the Kerr response of $CrPS_4$, we compute the complex Kerr parameters according to the equation

$$\psi_K = \theta_K + i\gamma_K = \frac{-\varepsilon_{xz}}{(\varepsilon_{xx}-1)\sqrt{\varepsilon_{xx}}}, \tag{1}$$

which is the standard expression for the polar geometry in the small-angle limit [48]. Here, the photon propagates along the *y* direction and describes a linearly polarized wave with the electric field along the *x* direction.

Figure 5 shows the real and imaginary Kerr parameters θ_K and γ_K, respectively, as a function of frequency. Both Kerr parameters oscillate about zero, displaying a quite sensitive dependence on the frequency of light. Specifically, θ_K and γ_K change sign at ≈2 eV, followed by several additional fluctuations about zero until a maximum in both signals is achieved ∼9 eV. Above 9 eV, the Kerr parameters vary more smoothly with frequency. Additionally, θ_K and γ_K appear to be completely out of phase for all frequencies studied. Such a line shape in the Kerr signal is quite different from bulk three-dimensional (3D) magnets, e.g., Fe, Co, and Ni, and more akin to other 2D magnets, e.g., $NiPS_3$ [42].

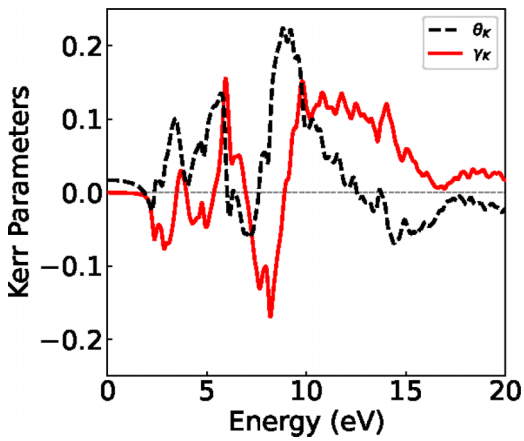

FIG. 5. The Kerr parameters of monolayer $CrPS_4$ as a function of energy.

VI. CONCLUDING REMARKS

In this paper, we have demonstrated that a first-principles parameter free treatment of the ground-state magnetic and electronic proprieties of the air-stable $CrPS_4$ 2D magnet is possible. Using the SCAN density functional, we find a major improvement over standard PBE and PBE+*U* approaches, at nearly the same computational cost. In this paper, we lay a firm foundation for the predictive exploration and design of heterostructures and devices composed of $CrPS_4$, mitigating the need for purely experimental efforts. Furthermore, the highly anisotropic cross-coupling between spin, charge, and lattice also provides a path toward multifunctional devices ideal for monolithically integrating into semiconducting substrates for efficient interfaces between logic-interconnect-memory sectors in emerging 3D logic-memory architectures.

ACKNOWLEDGMENTS

The work at Los Alamos National Laboratory (LANL) was carried out under the auspices of the U.S. Department of Energy (DOE) National Nuclear Security Administration under Contract No. 89233218CNA000001. It was supported by the LANL Laboratory Directed Research and Development Program, the Quantum Science Center, a U.S. DOE Office of Science National Quantum Information Science Research Center, and in part by the Center for Integrated Nanotechnologies, a DOE Basic Energy Sciences user facility, in partnership with the LANL Institutional Computing Program for computational resources. Additional computations were performed at the National Energy Research Scientific Computing Center (NERSC), a U.S. DOE Office of Science User Facility located at Lawrence Berkeley National Laboratory, operated under Contract No. DE-AC02-05CH11231 using NERSC Award No. ERCAP0020494. J.T.H. acknowledges support from the Institute of Materials Science at LANL under Subcontract No. 616898.

APPENDIX A: CHROMIUM MAGNETIC MOMENTS AS A FUNCTION OF WIGNER-SEITZ RADIUS

Figure 6 shows the Cr atomic magnetic moment as a function of the Wigner-Seitz radius (r_{WS}) or integration sphere. The black dotted line denotes the default value of r_{WS} defined in VASP, which yields a magnetic moment of 2.78 μ_B. Upon

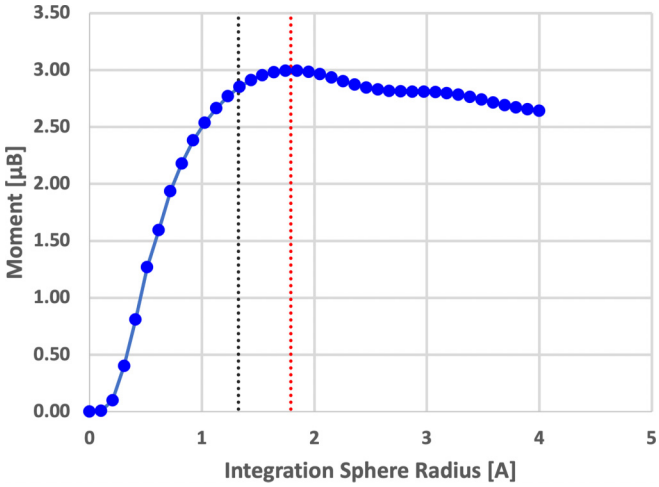

FIG. 6. The magnetic moment as a function of integration sphere radius of bulk $CrPS_4$ in the A-type antiferromagnetic (A-AFM) phase.

expanding r_{WS}, we find the magnetic moment to increase since the integration sphere encapsulates more chromium magnetic density. At $r_{WS} = 1.74$ Å, a maximum in the magnetic moment is found with a value of $3.00\,\mu_B$ (red dotted line). Moreover, as the integration sphere is expanded beyond the covalent radius of chromium, an admixture of sulfur density is included, thereby reducing the net effective moment. Note that the Cr moment for large r_{WS} values will depend on the coordination number and thus on the crystal structure.

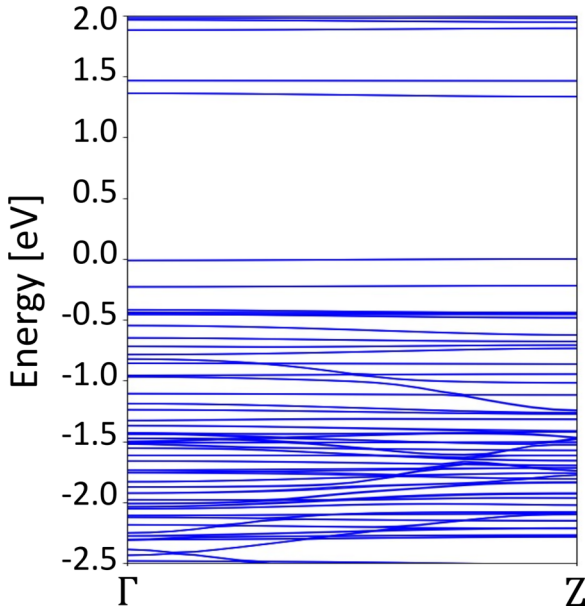

FIG. 7. Electronic band structure along Γ-*Z* in the Brillouin zone for bulk $CrPS_4$ in the A-type antiferromagnetic (A-AFM) phase.

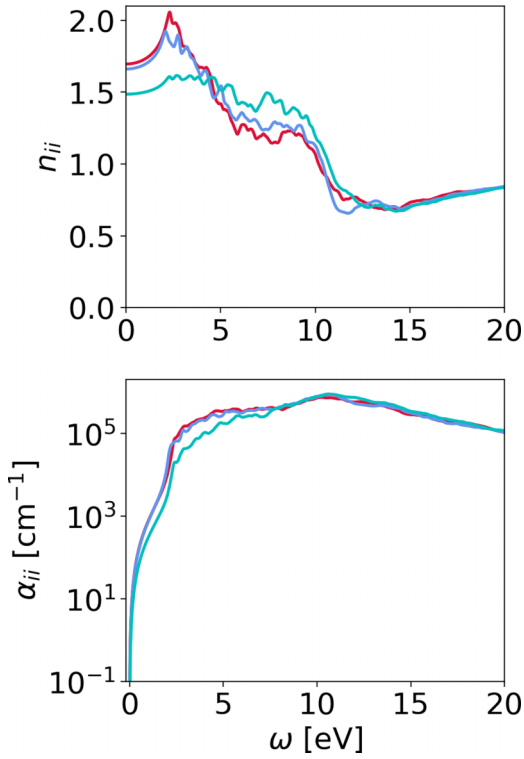

FIG. 8. Refractive index and optical absorption for monolayer $CrPS_4$ in the ferromagnetic (FM) phase. The red, blue, and teal lines are for the *xx*, *yy*, and *zz* components, respectively.

APPENDIX B: Γ-*Z* BAND DISPERSION

Figure 7 shows the electronic band structure along Γ-*Z* in the Brillouin zone for bulk $CrPS_4$ in the A-AFM phase. Most bands are essentially flat, with only a few valence states below −0.75 eV displaying a dispersive nature. This suggests the interlayer coupling in $CrPS_4$ is quite weak, rendering the atomically thin layers even in the bulk compound electronically isolated.

APPENDIX C: REFRACTIVE INDEX AND OPTICAL ABSORPTION SPECTRUM

Figure 8 presents the refractive index and optical absorption for monolayer $CrPS_4$ in the FM phase. The refractive index n_{ii} is related to the diagonal parts of the dielectric tensor by

$$n_{ii} = \sqrt{\frac{|\varepsilon_{ii}| + \Re\varepsilon_{ii}}{2}}, \tag{C1}$$

whereas the absorption coefficient:

$$\alpha_{ii} = \frac{2\omega k_{ii}}{c}, \tag{C2}$$

is proportional to the dielectric tensor through extinction coefficient:

$$k_{ii} = \sqrt{\frac{|\varepsilon_{ii}| - \Re\varepsilon_{ii}}{2}}. \tag{C3}$$

[1] M. Gibertini, M. Koperski, A. Morpurgo, and K. Novoselov, Magnetic 2D materials and heterostructures, Nat. Nanotechnol. **14**, 408 (2019).

[2] Y. Li, N. Zaki, V. O. Garlea, A. T. Savici, D. Fobes, Z. Xu, F. Camino, C. Petrovic, G. Gu, P. D. Johnson *et al.*, Electronic properties of the bulk and surface states of $Fe_{1+y}Te_{1-x}Se_x$, Nat. Mater. **20**, 1221 (2021).

[3] K. Kim, J. Seo, E. Lee, K.-T. Ko, B. Kim, B. G. Jang, J. M. Ok, J. Lee, Y. J. Jo, W. Kang *et al.*, Large anomalous hall current induced by topological nodal lines in a ferromagnetic van der Waals semimetal, Nat. Mater. **17**, 794 (2018).

[4] K. S. Burch, D. Mandrus, and J.-G. Park, Magnetism in two-dimensional van der Waals materials, Nature (London) **563**, 47 (2018).

[5] D. Shcherbakov, P. Stepanov, D. Weber, Y. Wang, J. Hu, Y. Zhu, K. Watanabe, T. Taniguchi, Z. Mao, W. Windl *et al.*, Raman spectroscopy, photocatalytic degradation, and stabilization of atomically thin chromium tri-iodide, Nano Lett. **18**, 4214 (2018).

[6] S. Calder, A. V. Haglund, Y. Liu, D. M. Pajerowski, H. B. Cao, T. J. Williams, V. O. Garlea, and D. Mandrus, Magnetic structure and exchange interactions in the layered semiconductor $CrPS_4$, Phys. Rev. B **102**, 024408 (2020).

[7] J. Son, S. Son, P. Park, M. Kim, Z. Tao, J. Oh, T. Lee, S. Lee, J. Kim, K. Zhang *et al.*, Air-stable and layer-dependent ferromagnetism in atomically thin van der Waals $CrPS_4$, ACS Nano **15**, 16904 (2021).

[8] L. Meng, Z. Zhou, M. Xu, S. Yang, K. Si, L. Liu, X. Wang, H. Jiang, B. Li, P. Qin *et al.*, Anomalous thickness dependence of Curie temperature in air-stable two-dimensional ferromagnetic $1T$-$CrTe_2$ grown by chemical vapor deposition, Nat. Commun. **12**, 809 (2021).

[9] A. Purbawati, S. Sarkar, S. Pairis, M. Kostka, A. Hadj-Azzem, D. Dufeu, P. Singh, D. Bourgault, M. Nuñez-Regueiro, J. Vogel *et al.*, Stability of the in-plane room temperature van der Waals ferromagnet chromium ditelluride and its conversion to chromium-interleaved $CrTe_2$ compounds, ACS Appl. Electron. Mater. **5**, 764 (2023).

[10] W. L. Huey, A. M. Ochs, A. J. Williams, Y. Zhang, S. Kraguljac, Z. Deng, C. E. Moore, W. Windl, C. N. Lau, and J. E. Goldberger, $Cr_xPt_{1-x}Te_2$ ($x \leqslant 0.45$): A family of air-stable and exfoliatable van der Waals ferromagnets, ACS Nano **16**, 3852 (2022).

[11] Q. Pei, X. Luo, G. Lin, J. Song, L. Hu, Y. Zou, L. Yu, W. Yong, W. Song, W. Lu *et al.*, Spin dynamics, electronic, and thermal transport properties of two-dimensional $CrPS_4$ single crystal, J. Appl. Phys. **119**, 043902 (2016).

[12] J. Lee, T. Ko, J. Kim, H. Bark, B. Kang, S. Jung, T. Park, Z. Lee, S. Ryu, and C. Lee, Structural and optical properties of single- and few-layer magnetic semiconductor $CrPS_4$, ACS Nano **11**, 10935 (2017).

[13] A. K. Budniak, N. A. Killilea, S. J. Zelewski, M. Syntnyk, Y. Kauffmann, Y. Amouyal, R. Kudrawiec, W. Heiss, and E. Lifshitz, Exfoliated $CrPS_4$ with promising photoconductivity, Nano Micro Small **16**, 1905924 (2020).

[14] P. Gu, Q. Tan, Y. Wan, Z. Li, Y. Peng, J. Lai, J. Ma, X. Yao, S. Yang, K. Yuan *et al.*, Photoluminescent quantum interference in a van der Waals magnet preserved by symmetry breaking, ACS Nano **14**, 1003 (2020).

[15] S. Kim, J. Lee, G. Jin, M. Jo, C. Lee, and S. Ryu, Crossover between photochemical and photothermal oxidations of atomically thin magnetic semiconductor $CrPS_4$, Nano Lett. **19**, 4043 (2019).

[16] S. Kim, J. Lee, C. Lee, and S. Ryu, Polarized Raman spectra and complex Raman tensors of antiferromagnetic semiconductor $CrPS_4$, J. Phys. Chem. C **125**, 2691 (2021).

[17] H. Zhang, Y. Li, X. Hu, J. Xu, L. Chen, G. Li, S. Yin, J. Chen, C. Tan, X. Kan *et al.*, In-plane anisotropic 2D $CrPS_4$ for promising polarization-sensitive photodetection, Appl. Phys. Lett. **119**, 171102 (2021).

[18] M. Shin, M. J. Lee, C. Yoon, S. Kim, B. H. Park, S. Lee, and J.-G. Park, Charge-trapping memory device based on a heterostructure of MoS_2 and $CrPS_4$, J. Korean Phys. Soc. **78**, 816 (2021).

[19] M. Riesner, R. Fainblat, A. K. Budniak, Y. Amouyal, E. Lifshitz, and G. Bacher, Temperature dependence of Fano resonances in $CrPS_4$, J. Chem. Phys. **156**, 054707 (2022).

[20] S. Kim, S. Yoon, H. Ahn, G. Jin, H. Kim, M.-H. Jo, C. Lee, J. Kim, and S. Ryu, Photoluminescence path bifurcations by spin flip in two-dimensional $CrPS_4$, ACS Nano **16**, 16385 (2022).

[21] G. Xu, D. Liu, S. Li, Y. Wu, Z. Zhang, S. Wang, Z. Huang, and Y. Zhang, Binary-ternary transition metal chalcogenides interlayer coupling in van der Waals type-II heterostructure for visible-infrared photodetector with efficient suppression dark currents, Nano Res. **15**, 2689 (2022).

[22] H. L. Zhuang and J. Zhou, Density functional theory study of bulk and single-layer magnetic semiconductor $CrPS_4$, Phys. Rev. B **94**, 195307 (2016).

[23] M. Joe, H. Lee, M. Alyoruk, J. Lee, S. Kim, C. Lee, and J. Lee, A comprehensive study of piezomagnetic response in $CrPS_4$ monolayer: Mechanical, electronic properties and magnetic ordering under strains, J. Phys.: Condens. Matter **29**, 405801 (2017).

[24] Q. Chen, Q. Ding, Y. Wang, Y. Xu, and J. Wang, Electronic and magnetic properties of a two-dimensional transition metal phosphorous chalcogenide $TMPS_4$, J. Phys. Chem. C **124**, 12075 (2020).

[25] J. Deng, J. Guo, H. Hosono, T. Ying, and X. Chen, Two-dimensional bipolar ferromagnetic semiconductors from layered antiferromagnets, Phys. Rev. Mater. **5**, 034005 (2021).

[26] J. Yang, S. Fang, Y. Peng, S. Liu, B. Wu, R. Quhe, S. Ding, C. Yang, J. Ma, B. Shi *et al.*, Layer-dependent giant magnetoresistance in two-dimensional $CrPS_4$ magnetic tunnel junctions, Phys. Rev. Appl. **16**, 024011 (2021).

[27] A. Louisy, G. Ouvrard, D. Schleich, and R. Brec, Physical properties and lithium intercalates of $CrPS_4$, Solid State Commun. **28**, 61 (1978).

[28] M. Lee, S. Lee, S. Lee, K. Balamurugan, C. Yoon, J. Jang, S. Kim, D. Kwon, M. Kim, J. Ahn *et al.*, Synaptic devices based on two-dimensional layered single-crystal chromium thiophosphate ($CrPS_4$), NPG Asia Materials **10**, 23 (2018).

[29] G. Kresse and D. Joubert, From ultrasoft pseudopotentials to the projector augmented-wave method, Phys. Rev. B **59**, 1758 (1999).

[30] G. Kresse and J. Hafner, *Ab initio* molecular dynamics for open-shell transition metals, Phys. Rev. B **48**, 13115 (1993).

[31] G. Kresse and J. Furthmuller, Efficient iterative schemes for *ab initio* total-energy calculations using a plane-wave basis set, Phys. Rev. B **54**, 11169 (1996).

[32] J. Sun, A. Ruzsinszky, and J. P. Perdew, Strongly constrained and appropriately normed semilocal density functional, Phys. Rev. Lett. **115**, 036402 (2015).

[33] R. Diehl and C. Carpentier, The crystal structure of chromium thiophosphate, $CrPS_4$, Acta Cryst. **B33**, 1399 (1976).

[34] W. Kohn and L. J. Sham, Self-consistent equations including exchange and correlation effects, Phys. Rev. **140**, A1133 (1965).

[35] A. Seidl, A. Görling, P. Vogl, J. A. Majewski, and M. Levy, Generalized Kohn-Sham schemes and the band-gap problem, Phys. Rev. B **53**, 3764 (1996).

[36] J. P. Perdew, W. Yang, K. Burke, Z. Yang, E. K. Gross, M. Scheffler, G. E. Scuseria, T. M. Henderson, I. Y. Zhang, A. Ruzsinszky *et al.*, Understanding band gaps of solids in generalized Kohn-Sham theory, Proc. Natl. Acad. Sci. USA **114**, 2801 (2017).

[37] J. W. Furness, Y. Zhang, C. Lane, I. G. Buda, B. Barbiellini, R. S. Markiewicz, A. Bansil, and J. Sun, An accurate first-principles treatment of doping-dependent electronic structure of high-temperature cuprate superconductors, Commun. Phys. **1**, 11 (2018).

[38] C. Lane, J. W. Furness, I. G. Buda, Y. Zhang, R. S. Markiewicz, B. Barbiellini, J. Sun, and A. Bansil, Antiferromagnetic ground state of La_2CuO_4: A parameter-free *ab initio* description, Phys. Rev. B **98**, 125140 (2018).

[39] K. Pokharel, C. Lane, J. W. Furness, R. Zhang, J. Ning, B. Barbiellini, R. S. Markiewicz, Y. Zhang, A. Bansil, and J. Sun, Sensitivity of the electronic and magnetic structures of cuprate superconductors to density functional approximations, npj Comput. Mater. **8**, 31 (2022).

[40] Y. Zhang, C. Lane, J. W. Furness, B. Barbiellini, J. P. Perdew, R. S. Markiewicz, A. Bansil, and J. Sun, Competing stripe and magnetic phases in the cuprates from first principles, Proc. Natl. Acad. Sci. USA **117**, 68 (2020).

[41] C. Lane, Y. Zhang, J. W. Furness, R. S. Markiewicz, B. Barbiellini, J. Sun, and A. Bansil, First-principles calculation of spin and orbital contributions to magnetically ordered moments in Sr_2IrO_4, Phys. Rev. B **101**, 155110 (2020).

[42] C. Lane and J.-X. Zhu, Thickness dependence of electronic structure and optical properties of a correlated van der Waals antiferromagnetic $NiPS_3$ thin film, Phys. Rev. B **102**, 075124 (2020).

[43] C. Lane and J.-X. Zhu, Landscape of coexisting excitonic states in the insulating single-layer cuprates and nickelates, Phys. Rev. B **101**, 155135 (2020).

[44] C. Lane and J.-X. Zhu, An *ab initio* study of electron-hole pairs in a correlated van der Waals antiferromagnet: $NiPS_3$, arXiv:2209.13051 (2022).

[45] J. Zaanen, G. A. Sawatzky, and J. W. Allen, Band gaps and electronic structure of transition-metal compounds, Phys. Rev. Lett. **55**, 418 (1985).

[46] J. L. Erskine and E. Stern, Calculation of the M_{23} magneto-optical absorption spectrum of ferromagnetic nickel, Phys. Rev. B **12**, 5016 (1975).

[47] J. Xia, Y. Maeno, P. T. Beyersdorf, M. M. Fejer, and A. Kapitulnik, High resolution polar Kerr effect measurements of Sr_2RuO_4: Evidence for broken time-reversal symmetry in the superconducting state, Phys. Rev. Lett. **97**, 167002 (2006).

[48] D. Sangalli, A. Marini, and A. Debernardi, Pseudopotential-based first-principles approach to the magneto-optical Kerr effect: From metals to the inclusion of local fields and excitonic effects, Phys. Rev. B **86**, 125139 (2012).